

## Modeling Quasar Microlensing

L. Ledvina and D. Heyrovský

Institute of Theoretical Physics, Faculty of Mathematics and Physics, Charles University, Prague, Czech Republic.

**Abstract.** Light from a distant quasar passing in the vicinity of a foreground galaxy gets deflected by its gravitational field. According to Fermat's principle several macro-images of the quasar can then be observed. In addition, the light may be affected by the gravitational field of individual stars moving in the lensing galaxy, creating multiple micro-images. We cannot resolve them because of their small angular separation, but we can observe an associated increase in the source flux due to microlensing. We use simulations to show how the prominent X-ray iron  $K_\alpha$  line is affected during the microlensing event. We describe in detail the underlying numerical integration involving divergent integrands.

### Introduction

The first article about gravitational lensing was published by *Einstein* [1936], but it took more than 40 years till the first gravitationally lensed quasar 0957+561 was discovered by *Walsh et al.* [1979].

In our model we assume a setting similar to the first lens: a distant bright quasar and a galaxy lying along the line-of-sight to the quasar. Passing light is bent in the gravitational field of the galaxy and few macro-images are created with a typical separation of several arcseconds. When the light corresponding to one of the macro-images passes through the stellar population of the lens galaxy, photons are bent in the gravitational field of individual stars and additional images with micro-arcsecond separation are created, leading to an increase in flux [*Schmidt and Wambsganss*, 2010]. This effect can be observed at various wavelengths. We are interested in the innermost area of the accretion disk which emits mostly in X-rays. One of the first candidates for X-ray microlensing was quasar MG J0414+0534 observed by *Chartas et al.* [2002].

Microlensing can be also used to estimate the size of the emitting area, differences in the size between the optical and the X-ray band emission radius [*Dai et al.*, 2010], the temperature profile of the disk [*Eigenbrod et al.*, 2008], and additional properties of the specific intensity spatial distribution from observations of line profile changes [*Chen et al.*, 2011].

### Microlensing model

The lens equation for an extended lens galaxy [*Schneider et al.*, 2006] is

$$\vec{\beta} = \vec{\theta} - \frac{D_{\text{ds}}}{D_{\text{s}}} \vec{\alpha}(\vec{\theta}), \quad \vec{\alpha}(\vec{\theta}) = \frac{4GD_{\text{d}}}{c^2} \int d^2\theta' \rho(\vec{\theta}') \frac{\vec{\theta} - \vec{\theta}'}{|\vec{\theta} - \vec{\theta}'|^2}, \quad (1)$$

where  $\vec{\beta}$  is the source position vector in the quasar plane,  $\vec{\theta}$  is the image position vector in the lens plane,  $\rho(\vec{\theta})$  is the surface mass density of the lens galaxy,  $D_{\text{ds}}$  is the angular-diameter distance between the quasar and the lens galaxy,  $D_{\text{s}}$  is the angular-diameter distance from the observer to the quasar and  $D_{\text{d}}$  is the angular-diameter distance from the observer to the lens. Deflection of light by the lens galaxy creates a flux amplification map in the quasar plane. The fine structure of the map in the vicinity of a given macro-image is determined by the local stellar population of the lens galaxy. The combined gravitational field of these stars forms a caustic network with characteristic scale comparable to the angular size of the quasar accretion disk. The local surface mass distribution  $\rho(\vec{\theta})$  can be approximated in a simplest model by a set of point masses. In *Ledvina* [2011] we described an algorithm for calculating these maps, with an

example shown in Fig. 1. The angular scale unit used in these maps is the Einstein radius

$$\theta_E = \sqrt{\frac{4GM}{c^2} \frac{D_{ds}}{D_d D_s}}, \quad (2)$$

where  $M$  is the average mass of a microlensing star in the lens galaxy.

The quasar is moving with respect to the amplification map, which implies variability in the observed photon flux

$$F_{\text{obs}}(\beta_1^0, \beta_2^0) = \int_{\text{disk}} I_{\text{obs}}(\beta_1, \beta_2) A(\beta_1 - \beta_1^0, \beta_2 - \beta_2^0) d\beta_1 d\beta_2, \quad (3)$$

where  $(\beta_1^0, \beta_2^0)$  is the position of the quasar accretion disk center. The amplification factor is  $A$ ;  $I_{\text{obs}}(\beta_1, \beta_2)$  is the photon specific intensity in the observer frame.

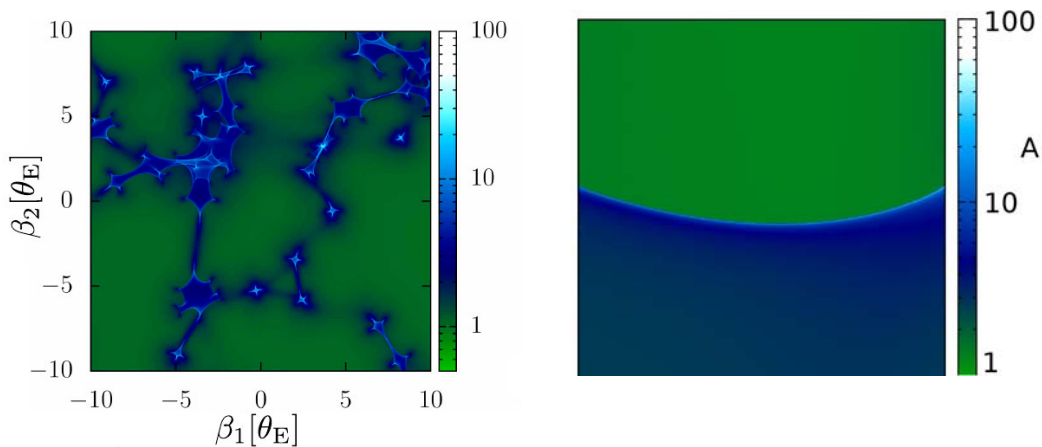


**Figure 1.** Left panel: Microlensing amplification map  $A(\beta_1, \beta_2)$  as a function of source position for a lens composed of stars with mean separation  $3.90 \theta_E$ . Right panel: Detail of amplification map showing fold caustic.

Two most common local structures of amplification maps are fold (see Fig. 1) and cusp caustics, along which the amplification peaks. Here we use the linear fold approximation [Chang and Refsdal, 1984], which is suitable because the X-ray emitting region of the disk is very small with respect to the characteristic scales of the amplification map. For the point-source amplification we have

$$A(\tilde{\beta}_1, \tilde{\beta}_2) = A_0 + \begin{cases} 0 & \text{for } \tilde{\beta}_1 \leq 0 \\ \sqrt{\frac{\alpha_0}{\tilde{\beta}_1}} & \text{for } \tilde{\beta}_1 > 0 \end{cases}, \quad (4)$$

where  $A_0$  is the amplification outside the fold,  $\alpha_0$  is the caustic strength and  $(\tilde{\beta}_1, \tilde{\beta}_2)$  are Cartesian coordinates rotated and shifted with respect to the coordinates  $(\beta_1, \beta_2)$  according to the fold position.

## Disk model

The disk emission models were kindly provided by Michal Dovčiak and Michal Bursa from the Astronomical Institute of the Czech Academy of Sciences. These models assume locally isotropic emission from the disk which drops with radial index  $q$ , consisting of prominent iron  $K_\alpha$  line radiation with delta-function shape at energy  $E_{\text{Fe}} = 6.4 \text{ keV}$ , and continuum radiation with spectral index  $\Gamma$ . Emitted photons are bent by the central Kerr black hole gravitational field and their energy  $E_{\text{em}}$  is multiplied by the g-factor,  $E_{\text{obs}} = gE_{\text{em}}$ , which includes gravitational redshift and the Doppler shift due to accretion-disk rotation [Dovčiak et al., 2004]. For the

specific intensity of the iron line and the continuum radiation emitted from the disk we can write

$$\text{iron line: } I_{\text{em}}^{\text{Fe}}(E_{\text{em}}) = I_0^{\text{Fe}} r^{-q} \delta[E_{\text{em}} - E_{\text{Fe}}], \quad (5)$$

$$\text{continuum: } I_{\text{em}}^{\text{cont}}(E_{\text{em}}) = I_0^{\text{cont}} r^{-q} E_{\text{em}}^{-\Gamma}, \quad (6)$$

where  $r$  is the Boyer–Lindquist radius and  $I_0$  are constants. The quantity  $I/E^2$  is conserved along the light ray (due to Lorentz covariance and the equivalence principle), from which we can obtain the specific intensity in the observer frame. A sample map of the iron line specific intensity is shown in Fig. 2.

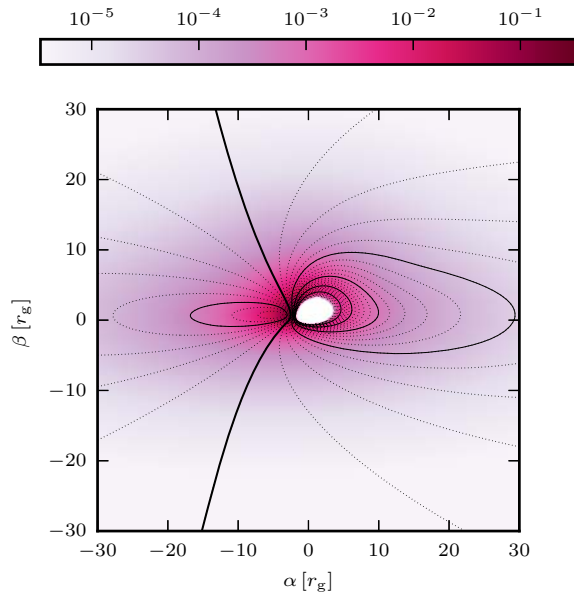


**Figure 2.** Observer-frame map of the iron  $K_{\alpha}$  line specific intensity distribution in the central part of the accretion disk,  $r_g$  is the gravitational radius. Coordinates  $\alpha, \beta$  are in the plane of the sky. Specific intensity is in relative units. Colour corresponds to specific intensity and contours corresponds to the g-factor. Lines are contours of the g-factor: bold for  $g = 1.0$  (higher values toward the left, lower toward the right), dotted with step 0.04, solid with step 0.2. Disk parameters: BH spin  $a = 1$ , radial index  $q = 3$ , inclination  $70^\circ$ .

### Microlensed flux: numerical integration

If we use equation (5) in (3) together with the transformation between emitted and observed specific intensity, we obtain the iron line specific flux at energy  $E_{\text{obs}} = g_0 E_{\text{Fe}}$

$$F(g_0) = \frac{I_0^{\text{Fe}}}{E_{\text{Fe}}} \int_{\text{disk}} g^3 r^{-q} A(\beta_1 - \beta_1^0, \beta_2 - \beta_2^0) \delta(g - g_0) d\beta_1 d\beta_2, \quad (7)$$

where  $r, g$  and  $A$  depend on  $\beta_1, \beta_2$  [for details see *Ledvina, 2014*].

For the numerical evaluation of this formula we use grid-based integration. We divided the disk into squares, on each of them we interpolate the terms  $g^3 r^{-q} I_0^{\text{Fe}} \sqrt{\alpha_0} / E_{\text{Fe}}$  and  $g - g_0$  bilinearly, and we rescale and shift coordinates to obtain integration boundaries  $(-1, 1)$ . We also split the amplification factor into the constant part and the part depending on position, calculating each separately. We describe here the algorithm for the latter part which is more difficult to calculate. The former part can be calculated by a similar algorithm assuming a constant denominator. For the observed flux from one square we get

$$F_{\text{sq}}(g_0) = \int_{-1}^1 \int_{-1}^1 \frac{a + bx + cy + dxy}{\sqrt{x \cos \psi + y \sin \psi + d_0}} \delta(A + Bx + Cy + Dxy) dx dy, \quad (8)$$

where  $x, y$  are new coordinates, angle  $\psi$  describes the caustic orientation,  $d_0$  is the perpendicular distance of the caustic from the origin, and  $a, b, c, d, A, B, C, D$  are constants of the bilinear approximations. The delta function determines the corresponding g-factor integration contour, which must pass through the square to give a non-zero contribution. We can perform the integration over  $y$ , which replaces  $y = -(Ax + B)/(Cx + D)$ , adds a multiplicative factor and changes the boundaries. One can easily prove that  $x \approx -D/C$  is usually outside the new integration boundaries (having  $|y| > 1$ ) except for rare pathological combinations of  $A, B, C, D$  with zero measure.

We cannot perform the second integration analytically and neither can we find the new integration boundaries exactly. Moreover, there might be more than one integration interval. Any integration boundary must be of one of the following types:

1.  $x$  coordinate of an intersection of the contour and the grid-square boundaries,
2.  $x$  coordinate of an intersection of the contour and the caustic.

We must find all candidates for boundaries, check if the points are upper or lower boundaries, and use all those of type 2 for the further calculation.

After the flux calculation for all grid squares we compare the flux in each square with the flux for a refined grid (relatively to the total flux). We accept the squares where the error is below the threshold. For the others (and their eight neighbors) we refine the grid by a factor of two. We have to refine also the neighbors to preserve continuity of the grid-based approximation. Fig. 3 shows an example of a refined grid.

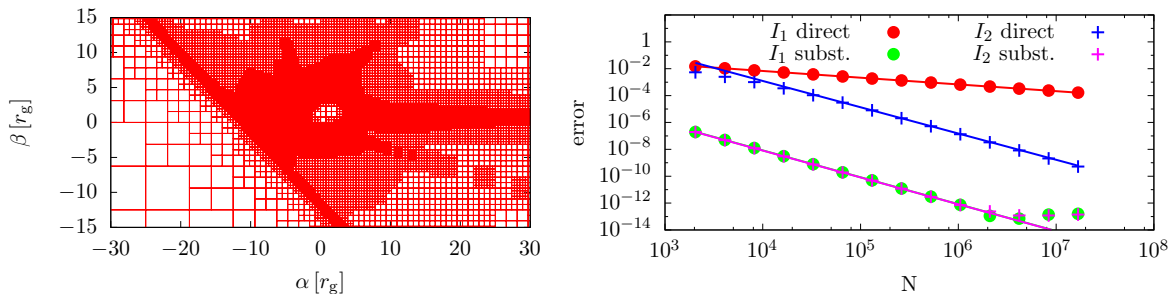


**Figure 3.** Left panel: Refined grid for flux calculation. The grid is more concentrated about the caustic (dense linear structure) and about the central black hole where the specific intensity is high. Right panel: Rate of convergence of integrals from equation (10) computed directly or using substitution (9) in cases  $c < a$  and  $c = a$ .

### Microlensed flux: divergent integrands

In this section we show how to improve the speed of convergence for improper integrals and proper integrals with integrand divergence just outside the integration interval.

Integration of the improper integral is described in *Press et al.* [2002], while the second type is not described there. Consider  $f(x)$  to be a smooth, bounded function, including higher derivatives,  $n < 1$  and  $c \leq a < b$ . The divergence-cancelling substitution is

$$\int_a^b \frac{f(x)}{(x-c)^n} dx = \frac{1}{1-n} \int_{(a-c)^{1-n}}^{(b-c)^{1-n}} f\left(c + t^{1/(1-n)}\right) dt. \quad (9)$$

We show that transformation (9) for  $c = a$  changes the asymptotic rate of convergence, while for  $c < a$  it improves the accuracy while preserving the convergence rate. For illustration we use the integrals

$$I_1 = \int_{-1}^0 \frac{dx}{\sqrt{(1-x)(1+x)}}, \quad I_2 = \int_{-0.9999}^0 \frac{dx}{\sqrt{(1-x)(1+x)}}. \quad (10)$$

For the integration we chose the open trapezoidal rule which converges as  $N^{-2}$  for proper functions. For the flux integration we use a 10-point Gaussian quadrature, but for illustrating the convergence rate trapezoidal quadrature is sufficient.

In Fig. 3 we compare the convergence rate of both integrals (10) when using direct integration and substitutions (9) with  $c = a$  and  $c < a$ . For the integral  $I_1$  substitution (9) (case  $c = a$ ) improves the asymptotic rate of convergence (from  $N^{-1/2}$  to  $N^{-2}$ ). For the integral  $I_2$  substitution (9) (case  $c < a$ ) decreases the error by five orders of magnitude maintaining  $N^{-2}$  convergence. For all methods the smallest possible error is the machine precision  $10^{-14}$ .

## Simulation results

Using the methods described above we simulate the time evolution of the spectrum  $F(g)$  for a caustic passing across the accretion disk. Contribution from the continuum radiation is calculated in a similar way as the line contribution. Results at four different times are presented in Fig. 4. The unit  $t_g$  is the time it takes the caustic to advance by  $1 r_g$  on the projected disk. In the first panel the caustic is far from the central part of the disk and the spectrum is affected by microlensing only weakly. In the last panel we see no additional features on the line, but the whole spectrum is amplified by a practically-constant factor. In the second and third panel we see significant changes in the iron-line profile. In observational data *Chartas et al.* [2012] also found changes in the iron line and *Chen et al.* [2012] presented non-typical shapes of the iron line which might be affected by microlensing.

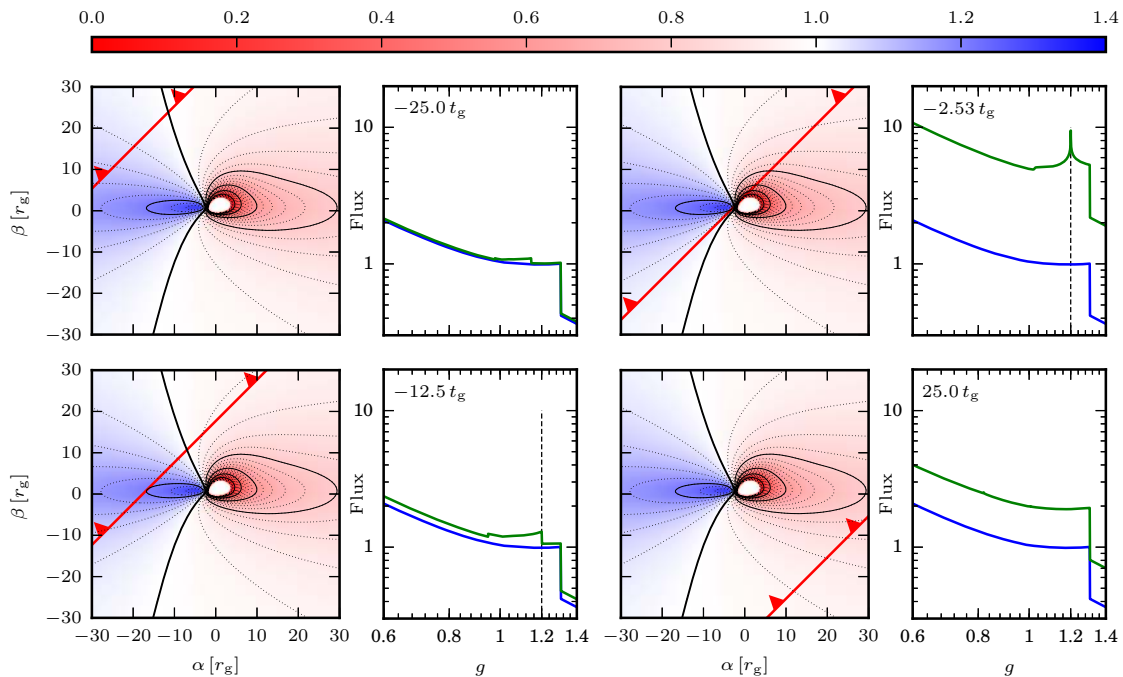


**Figure 4.** Time evolution of the quasar X-ray spectrum near the iron line during caustic crossing. Disk parameters are the same as in Fig. 2. The left panels show the color map and contours of the  $g$ -factor. The caustic is marked by the red line; its inner region by triangles. The right panels show the corresponding spectra with flux given in arbitrary units. Blue line marks the spectrum without lensing effect, green the lensed spectrum. The labels in the top left corners show the time measured from disk-center crossing. The dashed line in the second and third panels corresponds to the  $g = 1.2$  contour tangent to the caustic.

## Conclusion

We presented our algorithm for the calculation of the shape of the iron  $K_\alpha$  spectral line, but we can use it just as well for any other emission line. We illustrated a part of our integration technique showing how to increase the rate of convergence if the asymptotic behavior of the integrand is known. We also presented preliminary results indicating observable changes in the line profile.

Quasar microlensing is a new method for studying the central part of the accretion disk which allows us to resolve its surface-brightness distribution. With the described algorithm we can study microlensing-induced changes in the quasar spectrum and compare them with the observational data of *Chartas et al.* [2012].

**Acknowledgments.** This work was done in collaboration with Michal Dovčiak, Michal Bursa and Vladimír Karas from the Astronomical Institute of the Czech Academy of Sciences. This research was supported by Charles University grants GAUK 621912 GAUK 2000314, SVV-260211 and Czech Science Foundation grants GACR P209-10-1318 and GACR 14-37086G.

## References

- Chang, K. and Refsdal, S., Star disturbances in gravitational lens galaxies, *Astron. Astrophys.*, *132*, 168–178, 1984.
- Chartas, G., Agol, E., Eracleous, M., Garmire, G., Bautz, M. W., and Morgan, N. D., Caught in the Act: Chandra Observations of Microlensing of the Radio-loud Quasar MG J0414+0534, *Astrophys. J.*, *568*, 509–521, 2002.
- Chartas, G., Kochanek, C. S., Dai, X., Moore, D., Mosquera, A. M., and Blackburne, J. A., Revealing the Structure of an Accretion Disk through Energy-dependent X-Ray Microlensing, *Astrophys. J.*, *757*, 137, 2012.
- Chen, B., Dai, X., Kochanek, C. S., Chartas, G., Blackburne, J. A., and Kozłowski, S., Discovery of Energy-dependent X-Ray Microlensing in Q2237+0305, *Astrophys. J.*, *740*, L34, 2011.
- Chen, B., Dai, X., Kochanek, C. S., Chartas, G., Blackburne, J. A., and Morgan, C. W., X-Ray Monitoring of Gravitational Lenses with Chandra, *Astrophys. J.*, *755*, 24, 2012.
- Dai, X., Kochanek, C. S., Chartas, G., Kozłowski, S., Morgan, C. W., Garmire, G., and Agol, E., The Sizes of the X-ray and Optical Emission Regions of RXJ 1131-1231, *Astrophys. J.*, *709*, 278–285, 2010.
- Dovčiak, M., Karas, V., and Yaqoob, T., An Extended Scheme for Fitting X-Ray Data with Accretion Disk Spectra in the Strong Gravity Regime, *Astrophys. J. (Supp.)*, *153*, 205–221, 2004.
- Eigenbrod, A., Courbin, F., Meylan, G., Agol, E., Anguita, T., Schmidt, R. W., and Wambsganss, J., Microlensing variability in the gravitationally lensed quasar QSO 2237+0305 the Einstein Cross. II. Energy profile of the accretion disk, *Astron. Astrophys.*, *490*, 933–943, 2008.
- Einstein, A., Lens-Like Action of a Star by the Deviation of Light in the Gravitational Field, *Science*, *84*, 506–507, 1936.
- Ledvina, L., *Měření vlastností akrečního disku kvasarovým mikročočkováním*, Bakalářská práce, Univerzita Karlova v Praze, Matematicko-fyzikální fakulta, 2011.
- Ledvina, L., *Mapování akrečního disku kvasaru gravitačním mikročočkováním*, Diplomová práce, Univerzita Karlova v Praze, Matematicko-fyzikální fakulta, 2014.
- Press, W. H., Teukolsky, S. A., Vetterling, W. T., and Flannery, B. P., *Numerical recipes in C++ : the art of scientific computing*, Cambridge University Press, Cambridge, 2002.
- Schmidt, R. W. and Wambsganss, J., Quasar microlensing, *General Relativity and Gravitation*, *42*, 2127–2150, 2010.
- Schneider, P., Kochanek, C., and Wambsganss, J., *Gravitational Lensing: Strong, Weak and Micro*, Springer-Verlag, Berlin Heidelberg, 2006.
- Walsh, D., Carswell, R. F., and Weymann, R. J., 0957 + 561 A, B — Twin quasistellar objects or gravitational lens, *Nature*, *279*, 381–384, 1979.